

Coils for Large Standoff Relaxometry with Unilateral Magnets

Daniel M. Gruber^a, Sophia N. Fricke^a, Vanessa Lee^a, Bruce J. Balcom^b, and Matthew P. Augustine^a

^aDepartment of Chemistry
69 Chemistry Building
University of California, Davis
Davis, CA 95616 USA

^bDepartment of Physics
UNB MRI Centre
University of New Brunswick
Fredericton, New Brunswick, Canada

Abstract

Two types of radio frequency (rf) coils for linear array, unilateral magnets are described. These coils are designed to fully exploit the standoff distance of the unilateral magnet by placement directly on the magnet surface, a strategy that fails for normal surface coils used for magnetic resonance due to eddy current induced shielding by the conductive magnet surface. One design approach includes additional coils orthogonal to a standard loop or double D coil to reduce the rf field at the conducting magnet surface. The second design is a rectangular cross section solenoid coil mounted with the center axis of the coil parallel to the magnet surface. This geometry, when placed on a conducting surface, enhances the rf field produced in the sample region, outside of the solenoid coil. All of the coils are characterized using the ANSYS finite element modelling software. The best performing coils were constructed and magnetic resonance imaging (MRI) was used to experimentally confirm numerical predictions. Two experiments using these coils to perform large standoff relaxation measurements were accomplished to demonstrate the utility of these new coil geometries.

Keywords: Unilateral magnetic resonance; portable NMR; single-sided magnets

Declarations of interest: none

This research did not receive any specific grant from funding agencies in the public, commercial, or not-for-profit sectors.

1.0 Introduction

While nuclear magnetic resonance (NMR) has proven to be a powerful technique in chemical analysis, traditional methods typically require high radio frequency (rf) power and inflexible sample geometries that are not conducive to in situ analysis for manufacturing, processing, or field work. Unilateral magnets have been constructed and engineered to produce regions of relatively homogeneous magnetic field, well-displaced from the magnet surface that can be used for single-sided NMR[1,2]. These permanent magnets are much smaller than traditional superconducting or electro magnets allowing the NMR instrument to be portable. However, as the magnetic field is low and the sensors are typically deployed in dynamic, often electrically noisy environments, measurements typically have low signal-to-noise (S/N). A major impediment to unilateral magnetic resonance in connection with experiments requiring large standoff, or distance between the magnet and sample, is that the magnet interferes with the applied oscillatory rf magnetic field, B_1 , by supporting eddy currents. A surface coil may be lifted off of the magnet in order to mitigate eddy currents, however this comes at the expense of sample standoff distance from the magnet and probe assembly surface.

In the design of a unilateral magnet-based NMR sensor, the sources of the static magnetic field B_0 and the rf field B_1 must be considered. Several magnets have been designed to address the challenge of producing a homogeneous B_0 field displaced from a surface. One of the most well-known and commercially available single-sided sensors is the NMR-MOUSE [1]. This configuration consists of two opposed-polarity magnets that have been separated by just enough space to allow for a probe coil. The B_0 field produced by the NMR-MOUSE is transverse to the surface, while the B_1 produced by the probe coil is perpendicular. This design suffers very little from eddy currents in the magnet body and achieves a Larmor frequency of about 17 MHz, however the useful penetration depth is only a couple of millimeters.

Another attractive magnet design is the cylindrical magnet array [2]. This “barrel” magnet involves several stacked ring magnets and a cylindrical bar magnet placed in the center of the ring stack. The position of the cylindrical magnet is adjustable and used to establish the homogeneous region of the B_0 field. The static field in this configuration is perpendicular to the surface, while a figure-eight or “double D” (DD) style probe coil placed on top of the magnet provides a B_1 field transverse to the surface. This design has resulted in a homogeneous sensitive region ca. 1.5 cm above the surface, with a Larmor

frequency of ca. 5 MHz. Again this geometry does not suffer from eddy current formation as the majority of the DD coil is above the solid cylinder bar magnet that is depressed in the magnet rings.

A linear magnet array was created based on the idea of a solid, sideways bar magnet [3]. Here, a bar magnet is placed on its side, so that the static magnetic field is transverse to the surface. That bar magnet is then split into left and right halves and separated, leaving an inverted saddle region in the B_0 field above the surface. Then, a smaller bar magnet, aligned in the same direction as the first two pieces, is inserted between the halves, and its position may then be adjusted for fine tuning the distance of the homogeneous saddle region from the surface, similar to the cylindrical magnet array described above. Unlike the magnets previously described, in which the magnetic material is separated and pushed away from the sample region, this design allows for all of the magnetic material to be collocated as one solid volume next to the sample region, which results in a stronger and larger homogenous volume while using less material. The linear magnet array has produced magnetic fields with similar characteristics as the cylindrical magnet array, however with a much simpler design and while using approximately 20% less magnetic material, making them significantly lighter and less costly. Additionally, the solid nature of the construction of these magnets makes them less susceptible to temperature-induced field drift.

The linear magnet arrays are extremely attractive for industrial applications where portable sensors are needed to study materials well separated from the magnet surface by packaging, pipes and other sealed containers. However, the same feature that gives these magnets their desirable qualities, namely that they are essentially solid blocks of magnetic material, creates a significant problem for probe coil design when applications requiring the large standoff that these magnets offer are encountered.

Consider the usual linear unilateral magnet geometry with either a single circular loop or DD coil as shown in Fig. 1. In this figure, and throughout the remainder of this manuscript, the \hat{z} , \hat{h} and \hat{w} unit vectors respectively describe the direction of the static magnetic field in the homogeneous volume, the displacement off the magnet surface and the final orthogonal direction across the width of the magnet. With this convention, the coil is displaced from the magnet surface by the distance h_1 and the coil is separated from the homogeneous sample volume by the distance h_2 . A single magnetic flux line for the unilateral magnet is shown and the direction of the rf field offered by the loop or DD coil are indicated at the position of the homogeneous sample volume. It should be clear from Fig. 1 that h_1 must be minimized

in order to fully utilize the standoff and large homogeneous sample volume produced by the unilateral magnet. It is this requirement that introduces complications to the performance of the loop and DD coils typically used for physically localized imaging and single-sided NMR. Figure 2(a) describes what happens when a loop in the z-w plane producing an rf magnetic field is placed close to a conducting surface also in the z-w plane. Here an applied rf current, I , in the loop produces a primary rf magnetic field B_1 that induces eddy currents in the conductor I_{eddy} . It is these eddy currents that produce a secondary magnetic field B_{eddy} that subtracts from and thus reduces the effective primary field. This effect reduces both the size and homogeneity of the applied primary field. An appreciation for the severity of this effect at 5 MHz can be obtained from the magnetic field plots in Figs. 2(b) and (c) for a simple current loop of radius $R = 2$ cm held above a flat copper surface. The solid lines in both plots confirm expectations in the absence of a conducting surface where $h_1 > 4$ cm. The plots in Fig. 2(b) as a function of distance from the center of the coil r calculated at $h_2 = 1$ cm or at half the loop radius above the loop recovers the expected field homogeneity. Both the amplitude and the radial homogeneity are spoiled when the conducting surface is moved closer to a practically useful $h_1 = 2$ mm displacement as shown by the dashed line in Fig. 2(b). A similar performance reduction is also observed for the on axis field at $r = 0$ as a function of displacement h_2 from the surface of the coil. Again, the reduced field profile for $h_1 = 2$ mm offset is shown as the dashed line. Although just the magnetic field component normal to the loop and conducting surface in the \hat{h} direction is shown Fig. 2, it should be clear that the radial component of the field suffers from the same eddy current induced reduction and that these effects are just as severe for the DD coil.

There are three ways to circumvent the negative effects introduced by the conducting magnet surface on the primary field of a surface coil. One obvious approach mentioned above is to sacrifice unilateral magnet penetration depth by using simple loop or DD coils displaced by $h_1 > R$ from the magnet surface. In this configuration, eddy currents are minimized and changes to the applied primary field amplitude and homogeneity are reduced. This work considers two other practical approaches that minimize h_1 with the goal of placing the rf coil directly on the magnet surface. In this way the sample standoff distance of the unilateral magnet is fully exploited. The first idea avoids the production of eddy currents in the magnet by adding an array of coils to cancel or “buck” the field below a loop or DD coil to zero. This approach can have the benefit of adding rf field in the sample region above the loop or DD coil.

The second, more robust idea uses coils with magnetic flux lines that do not impinge the magnet surface. The following sections describe and mathematically and experimentally characterize these “bucked” and “fringe” coils in detail with the goal of identifying the best coil geometry for accomplishing large standoff NMR with linear unilateral magnets.

2.0 Materials and Methods

The rf magnetic field profiles shown in Figs. 2(b) and (c) were calculated with Matlab™ using the analytical results presented in Moser [4]. The asymmetry of the bucked coils, fringe coils and conducting plane encountered in this study, and the complexity that they introduce to the Maxwell equations required that the ANSYS AIM (Cannonsburg, PA) finite element, three dimensional differential equation solver be used for coil performance comparisons.

Four coils were constructed to experimentally test the predictions of the numerical models by magnetic resonance imaging the rf excitation field above the coils with and without a conducting plane. The first coil is a 6 turn, 3.5 cm side length square coil. The inductance and resistance of this simple surface coil are $L = 2.98 \mu\text{H}$ and $R = 0.2 \Omega$. A variant of this 3.5 cm square surface loop with two orthogonal, 3.5 cm x 0.63 cm rectangular bucking coils mounted on opposing sides of the square loop was also built. The square surface loop in this case had 3 turns while each rectangular bucking coil had 9 turns yielding combined $L = 5.25 \mu\text{H}$ and $R = 0.4 \Omega$ values. The $L = 9.38 \mu\text{H}$, $R = 0.4 \Omega$ fringe coil used here involved wrapping 33 turns onto a 2 cm long, 3.5 cm wide, 0.63 cm thick support. To be clear, the coil is wrapped around the “long” or “longitudinal” axis and the width of the coil is typically greater than the length. The coil wraps were continuous along the 2 cm long axis so that the final coil resembles a smashed solenoid coil. Finally, a split fringe coil, involving two 13 turn, 1.8 cm long, 3.5 cm wide, 0.63 cm thick fringe coils separated on the long axis by 1.5 cm was constructed with $L = 4.10 \mu\text{H}$ and $R = 0.4 \Omega$.

Mineral oil and laundry detergent samples were obtained from Safeway and used as received. All NMR data were obtained with a Tecmag (Houston, TX) Redstone spectrometer and three separate magnets were used in this study. Magnetic resonance images of the rf fields produced by the four model surface coils were obtained at a 4 MHz ^1H Larmor frequency with a 0.09 T SMIS imaging electromagnet. All of the images were created using a two rf pulse spin echo pulse sequence, with frequency encoding

along the z direction and phase encoding along the x and y directions. In all cases the pulsed field gradients were adjusted to provide 128 x 48 x 48 points in the z, x and y directions (\hat{z} , \hat{h} and \hat{w}) and an associated 12.8 cm x 12.8 cm x 12.8 cm field of view. The pole face gap in the SMIS magnet is large enough to allow a 4 inch diameter, 800 mL beaker of mineral oil to be placed directly on top of the bucked or fringe coils in the homogeneous region of the static magnetic field. In this way, simply sliding an aluminum plate, cut to the surface size and shape of a 3-magnet linear array, under the coil and beaker complex emulates the surface of a unilateral magnet. The portable unilateral magnet used in this study was the WA-1 built by Balcom, et. al. at the University of New Brunswick. It is a 18 cm x 11 cm x 7 cm, 0.05 T unilateral three permanent magnet array with a homogeneous sweet spot approximately 2.5 cm off the magnet surface that provides a 2.27 MHz ^1H Larmor frequency. This magnet along with the coil was sealed into a copper shielded, waterproof, Pelican™ case so that the sensor can be used on a benchtop or dunked into a liquid sample. All observed transverse relaxation time constants, T_2^{obs} , were obtained the Carr-Purcell-Meiboom-Gill (CPMG) pulse sequence [5][6]. Typical $\pi/2$ rf pulse and echo delay times were 18 μs and 1.046 ms respectively in the CPMG pulse sequence.

3.0 Results and Discussion

3.1 Calculations and Images

One way to mitigate the rf field profile changes introduced by the conducting plane shown in Fig. 2(a) for a circular loop, is to include additional coils that minimize the rf field impinging on the conducting surface. This concept is best understood by instead considering a square instead of a circular surface loop. The field in the center of this square loop in the z-w plane is in the \hat{h} direction. The addition of two rectangular, counter-wound secondary loops on either side of, below, and orthogonal to the primary square loop in the h-w plane yields rectangular loop centered fields pointing in the positive and negative \hat{z} direction. It is the dipole nature of these loop fields that add to the field above the square loop and subtract from the field below the square loop. The reduced field below the two rectangular coil, bucked square coil complex concomitantly reduces eddy current formation on the conducting surface. The more complicated geometry of a DD coil in the z-w plane with one added rectangular bucking coil in the h-z plane is shown in Fig. 3. The two square, counter-wound surface loops produce the primary field B_1 while

the added orthogonal bucking coil yields B_{buck} . It should be clear from Fig. 3 that the field amplitude above the DD z-w plane is $B_1 + B_{\text{buck}}$ while below it is $B_1 - B_{\text{buck}}$. It is the size, the number of turns, the placement and the number of bucking coils that are adjusted to minimize $B_1 - B_{\text{buck}}$ and thus eddy current formation at the conducting surface.

This simple idea was tested for a square loop and DD coil using the ANSYS modeling software and the results are provided in Fig. 4. The two-dimensional rf field plots show the coil in the z-w plane as black lines and the magnitude of the magnetic field produced by the coils perpendicular to the \hat{z} direction in the h-w plane at $z = 0$ or the coil center. The rf field plots in the left and center columns respectively correspond to the coil residing in free space and having the top of the coil $h_1 = 6$ mm above a flat conducting surface. The plot in the right column shows how the rf field behaves with standoff distance h_2 from the coil surface, with $w = z = 0$.

Figure 4(a) reproduces the results shown in Fig. 2 for the circular loop coil but instead uses a 35 mm side length square coil. The dumbbell shaped intensity pattern in the h-w plane in the plot in the left column in Fig. 4(a) is collection of responses analogous to the solid line for one value of h_2 in Fig. 2(b). Introduction of the conducting surface clearly reduces the field intensity provided by the coil as evidenced by the darkening of color in the plot in the center of Fig. 4(a) in comparison to the picture in the left column. Again this purely numerical result is consistent with the analytical prediction shown as the dashed line in Fig. 2(b). The same consistent comparison between numerical and analytical results is revealed in the standoff performance as well. This is demonstrated by comparing the square coil results in the right column in Fig. 4(a) to the circular loop results in Fig. 2(c). In both figures the solid line corresponds to free space and the dashed line describes the conductor attenuated results. The vertical gray line shown in the standoff distance plot in Fig. 4(a) is a conservative estimate of the position of the homogeneous static magnetic field volume established by the unilateral magnet. A comparison of the rf field gain or reduction at this position serves as one performance metric for conducting shield compensation as a function of coil geometry. In this first case of a square loop, the rf field 2 cm from the coil surface is reduced by 42 % when the conducting plane is introduced. This rf field reduction is improved by almost a factor of two when two counter-wound bucking coils are introduced on opposing sides of the flat square coil in the h-z plane as shown in Fig. 4(b). The added bucking coils introduce two interesting features to the rf field profile. First,

comparison of the first two columns in Fig. 4(b) to (a) suggests that the rf field volume is higher. This is, however, due to the fact that the field reported in Fig. 4(b) includes the bucking coils. Second, comparison of the standoff distance plots in the right column of Figs. 4(a) and (b) suggest that the added bucking coils accomplish their goal as the 2 cm standoff attenuation factor drops to 25 %, a number less than the 42 % reduction observed for the standard square surface coil.

Figures 4(c) and (d) provide a similar comparison of a DD coil and a single coil bucked DD coil. The primary DD coil in this case is of similar size to the square coil described above. Although not as severe as for the square coil, the rf field of the DD coil is reduced by 28 % at the $h_2 = 2$ cm standoff by the addition of the conducting plane. Again, the added bucking coil reduces the conducting plane attenuation by roughly a factor of two to 12 % at the $h_2 = 2$ cm standoff distance.

The comparison of the performance of the standard square loop and DD coils to the bucked versions in Fig. 4 strongly suggests that the core idea of reducing the rf field at the conducting surface by adding orthogonal, counter-wound coils improves the rf standoff distance by about a factor of two. Further improvements require either making the orthogonal bucking coils larger, adding more bucking coils or reducing the size of the primary square loop or DD coil to more effectively match the bucking and primary rf fields. Unfortunately, the addition of larger bucking coils underneath the primary square loop or DD coil is not an option here as that design change reduces the standoff distance because the coil complex will be lifted from the unilateral magnet surface. Adding more bucking coils is also not an attractive option as the produced fields become more complicated while not offering much improvement in metal shielding compensation. Reducing the primary square loop or DD coil size so that the existing bucking coils shown in Fig. 4 more effectively match the primary field is also not desirable as the overall measured homogenous static magnetic field volume is less, the NMR signals are smaller and experiment time is increased.

Instead of attempting to cancel the rf field impinging on the unilateral magnet surface, another option considers inductors on metal surfaces that yield flux lines that do not intersect the conducting surface. The solenoid coil shown in Fig. 5 satisfies this requirement. The two flux lines shown in black and labelled as B_1 describe the primary field of the solenoid coil. The flux lines above the center axis of the solenoid in the \hat{w} direction should be immune to the conductor shielding as these flux lines do not

intersect the unilateral magnet surface. The flux lines below the center axis of the solenoid do intersect the conducting surface, however, because of the coil-to-conducting surface geometry, these flux lines generate eddy currents I_{eddy} that have the surprisingly advantageous effect of generating a field B_{eddy} that adds to the field B_1 above the solenoid coil in the measurement region. The standard solenoid coil with circular cross section is not desirable for this application as the standoff distance is not maximized. To take advantage of the rf amplification offered by the conducting surface suggested by Fig. 5 while maximizing standoff distance h_2 , the solenoid coil is flattened to create an ellipsoidal or rectangular cross section solenoid coil. This smashed solenoid coil is referred to as a fringe coil to distinguish it from a standard circular cross section solenoid coil. The nomenclature was also chosen because the active volume is outside of the coil in the fringe case while for a standard solenoid coil in NMR the active volume is inside of the coil.

The plots shown in Fig. 6(a) describe the performance of a 1 cm long, 3.5 cm wide, 0.5 cm thick fringe coil with its center axis in the \hat{w} direction in free space in the left column and above the conductor in the center column. The top row in Fig. 6(a) shows the rf field profile in the h-w plane at $z = 0$ while the bottom row displays the rf field profile in the h-z plane at $w = 0$. These plots suggest that the rf field above the fringe coil is not attenuated by the conducting surface. Rather, as predicted by the standoff distance summary in the right column of Fig. 6(a) and by Fig. 5, the rf field in the measured sample volume at $h_2 = 2$ cm from the unilateral magnet surface increases by 43 %.

The standard fringe coil is designed to obtain signals directly above and outside of the coil. However, both common knowledge and the calculations shown in the top row of Fig. 6(a) suggest that the rf field at either end of the fringe coil near the rectangular openings is more intense than the rf field outside and above the fringe coil. It is for this reason that the opposed, counter-wound fringe coil was created. The performance of this split fringe coil is shown in Fig. 6(b). The two 1.8 cm long, 3.5 cm wide, 0.63 cm thick counter-wound coils are separated by 1.5 cm. The top plots in Fig. 6(b) show the rf field profile in the h-w plane at the $z = 0$ center of the split fringe coil while the lower plots display the rf field profile in the h-z plane at the $w = 0$ center of the split fringe coil. Finally, the plot in the far right column shows the rf standoff performance of the fringe coil. Once again, the signal at $h_2 = 2$ cm is increased, this time by about 44 %.

A comparison of the theoretical predictions made in Figs. 4 and 6 suggest that the fringe and split fringe coils offer the best immunity to unilateral magnet conducting surface-induced rf attenuation. An experimental comparison of the performance of these two fringe coils to a standard square loop is shown in Fig. 7. Here, the images in the left column are without a conductor while an aluminum plate is placed 6 mm below the top of the coil in the right hand column. The number included in the lower right corner of the right column image is the ratio of the maximum signal obtained with the conductor in place to that same maximum signal in free space. The square loop performs as expected, providing a reduction of about a factor of two upon placement on the conducting shield. More important is the gain in rf field amplitude for the fringe and split fringe coils predicted in Fig. 6 and experimentally observed in Fig. 7. Another interesting feature of these results is that the standoff distance of the fringe and split fringe coils improves slightly upon adding the conducting surface underneath the coil. Again, this is anticipated by the predictions made in Figs. 5 and 6.

3.2 Unilateral Magnet-Based Characterization

Both calculation and experiment suggest that the fringe coils provide the largest rf field intensity or standoff distance of the coils considered here. The fringe and the split fringe coils were further characterized with two additional experiments. Both experiments use the 0.05 T (2.27 MHz) WA-1 unilateral magnet and the same fringe coils that were used to obtain the rf excitation images in Fig. 7(c). The 3.5 cm width of these fringe coils was chosen so that they could be inserted easily into the 3.6 cm rectangular groove created by the depressed central bar magnet in the three magnet linear array.

In the first set of characterization experiments, a large beaker of mineral oil was placed on top of the magnet and coil, and T_2^{obs} values as a function of beaker-to-coil distance (h_2 in Fig. 1) were obtained using the CPMG pulse sequence. This experiment was duplicated for both coils on the same magnet. The average and standard deviation of the T_2^{obs} values obtained for beaker displacements ranging from 6 mm to 2.1 cm are shown in Fig. 8. As expected for high noise environments, T_2^{obs} values appeared shortened, but stabilized once a sufficiently high S/N was achieved. Moreover, the error increases with displacement, again as expected, since the S/N also significantly decreases with greater displacement from the magnet. Fig. 8(a) shows the results from the flat fringe coil performing well at short standoff distances, but as the

sample starts to approach the edge of the magnet sweet spot, uncertainty increases until finally being unable to fit the decay due to high S/N. Fig. 8(b) shows the results from the split fringe coil, which performs superiorly for all standoff distances, and even sufficiently for a decay fit at a standoff distance of 2.1 cm, which was not able to be achieved by the flat fringe coil at this distance and number of averages. It is important to note that the same number of acquisitions were used for all of the measurements shown in Fig. 8, and that the S/N and hence the uncertainty at large standoff distances will be improved by signal averaging.

The second set of characterization experiments considered the strength of the B_1 rf field produced by the two fringe coils as determined from a nutation experiment. Again, a large beaker of mineral oil was placed on top of the magnet and coil. This time the amplitude of a single spin echo is tracked as a function of the rf pulse length at a fixed applied rf amplitude. The results are shown in Fig. 9(a) for the flat fringe, and Fig. 9(b) for the split fringe coil. The plots show the integrated magnitudes, imaginary data, and real data in successively lighter shades of grey, respectively, with the width of the lines representing the 95% confidence interval for each set of data. The first peak appears at one-half the period of the Rabi frequency. For the flat fringe, this is at approximately 50 microseconds, giving a Rabi frequency of 10 kHz, while the split fringe integration peaks at approximately 35 microseconds, giving a Rabi frequency of 14.3 kHz. The fact that the Rabi cycling does not continue after the first cycle is indicative of the inhomogeneous nature of the system, such that the spins are actively dephasing during the pulse itself.

3.3 Unilateral Magnet Applications

The superb performance of the split fringe coil in all characterization efforts prompted two challenging real-world applications to confirm this prediction. In the first application, the coil and magnet assembly, in its copper lined, sealed, Pelican™ case were dunked into a 5 gallon bucket of Gain™ doped with CuSO_4 , a setup chosen to emulate observation in a large format vat mixer or other industrial setting. The photographs in Figs. 10(a) show the unilateral magnet and coil in the open case (left), as well as dunked in Gain™ for its experimental configuration (upper-right). With the encased magnet and coil submerged in the bucket of doped Gain™, CPMG decay transients were obtained with $T_2^{\text{obs}} = 16$ ms shown in Fig. 10(b). These experiments took 2.8 minutes for 256 transients, and achieved a S/N of 147.6.

The second application considers the in-situ exploration of natural products or crops. Unilateral magnetic resonance has previously been used to measure the moisture content of wood, using a similar magnet [7]. A small piece of tree branch, approximately 1 inch in diameter, was obtained and sealed in a plastic bag between experiments to prevent drying. This stick was then placed over the sweet spot of the sealed WA-1 magnet and split fringe coil, as shown in the lower-right of Fig. 10(a). The results are shown in Fig. 10(c), with 1735 transients in 10 minutes, $T_2^{\text{obs}} = 3.5$ ms and 20 ms, at a S/N of 1046.94 was able to be obtained, corresponding to the signal from water in the cells and lumen, respectively. This is in reasonable agreement with previous observations carried out with various wood types [8][9]. This illustrates the potential for this coil and magnet to be used in similar investigations, even when the sample size is small, such as a branch. This is remarkable for such a small sample volume, compared to that of immersing the magnet and coil in sample, as described above.

4.0 Conclusion

The availability of unilateral magnets has broadened the types of problems that can be studied with NMR spectroscopy and relaxometry. Instead of being restricted to samples that must fit inside of a glass tube or ceramic rotor, these single-sided magnets allow samples of almost any geometry or size to be studied with NMR. The primary challenge of single-sided NMR has been designing magnets that provide large homogeneous static magnetic field volumes significantly displaced $h_1 + h_2 > 2$ cm from the magnet surface while ensuring that the field strength is large enough to provide signals with minimal signal averaging. To this end, the linear unilateral magnet arrays mentioned above appear to best meet this challenge as the magnet material is located as close to the sample as possible. The consequence of this magnet choice is that the full standoff distance offered by the linear array is not fully exploited as the use of standard surface rf coils themselves require an offset from the magnet surface due to eddy current formation.

This work specifically addressed the eddy current shielding problem by proposing two coil geometries. Numerical simulations of the rf field provided by the square loop and DD coils suggest that eddy current shielding can be attenuated by adding orthogonal bucking coils to the primary coil. To make these coils experimentally useful, either the size of the orthogonal bucking coils must be increased or the

size of the primary square loop or DD coil must be decreased. Both of these options are not attractive for real world experiments. Another alternative not explored here would be to consider an array of small, bucked, primary coils. Although the rf field profile off the surface of the coil is complicated, the approach should yield useful, measureable NMR signals with an experimentally practical standoff. A much better approach identified here is to use a fringe or split fringe coil. These coils are essentially flattened solenoids and the signal is obtained from outside of the rf coil, in the “fringe” region. The interesting feature of this family of coils is that the conducting surface enhances the rf field at the homogenous sample volume.

Two geometries of fringe coils, a simple “flat fringe” coil and an opposed “split fringe” coil, were constructed and two characterization experiments were performed to compare the best-in-class fringe coils. These characterizations involved sequential experiments with the sample successively spaced farther from the magnet surface, as well as a nutation experiment, which indirectly measured the rf power in the sample. In this way the maximum sample standoff, T_2^{obs} values and Rabi cycling times were obtained at a h_2 around 2 cm standoff for a beaker of mineral oil. The fringe geometries as a class were predicted and observed to perform better than the traditional and bucked primary coil geometries, and in all characterization experiments, the split fringe coil outperformed the flat fringe coil. Further experiments with real-world applications were also conducted using the better performing split fringe coil. These experiments involved the immersion of the magnet and coil assemblies into laundry detergent, as well as the investigation of a small stick placed on top of the assembly. The split fringe coil was able to easily perform in both environments, even discerning multiple relaxation components in the stick.

All experiments yielded positive results, typically with just over two minutes of signal averaging, which is more than adequate for field use, the split fringe coil is the simplest coil array that largely matches the spatial profiles of B_1 to B_0 within the sensitive region of the magnet. Adding more fringe coils to make a cross or star pattern involving fringe coil building blocks of varying size will likely match the B_1 and B_0 fields better, and lead to greater standoff distance and larger signals, however for the magnets used in this study, this would preclude the advantage of utilizing the depressed notch in the center of the magnet array, leading to slightly reduced useable standoff distance. Still, it is these larger signals that reduce experiment time, an important parameter when the rapid throughput measurements commonly

encountered in industrial problems are required. Future work will involve exploring the multiple split fringe coil geometries.

Another strategy for reducing the eddy current problem that has been suggested is to include a layer of ferrite magnet between the magnet array and the coil. The resistivity of ferrite is much greater than that of neodymium alloys and this should in theory mitigate eddy currents without significantly reducing B_0 field strength. This idea does however neglect the fact that resistivity is magnetic field dependent [10][11]. Indeed, the beneficial conductive properties of ferrite experienced at zero field vanish at NMR useful magnetic field strengths. At the elevated field, the resistivity of ferrite more closely resembles that of copper and aluminum. Furthermore, as explained earlier in the theory section, eddy currents actually become advantageous when using the fringe coil geometry, and so reducing them in fact reduces the benefits of the fringe coils as well. Therefore the strategy was not investigated further. Finally, we note that, through the interaction of the reactive field and the incident B_1 field, the B_1 shape can also be changed by modifying the conducting surface curvature, an effect not studied here as all of the conducting surfaces were considered to be flat.

References

- [1] Eidmann, G & Savelsberg, R & Blümler, Peter & Blümich, Bernhard. (1996). The NMR MOUSE, a mobile universal surface explorer. *Journal of Magnetic Resonance Series A*. 122. 104-109. 10.1006/jmra.1996.0185.
- [2] Utsuzawa, Shin & Fukushima, Eiichi. (2017). Unilateral NMR with a barrel magnet. *Journal of Magnetic Resonance*. 282. 10.1016/j.jmr.2017.07.006.

- [3] E Marble, Andrew & Mastikhin, Igor & G Colpitts, Bruce & J Balcom, Bruce. (2007). A Compact Permanent Magnet Array with a Remote Homogeneous Field. *Journal of magnetic resonance*. 186. 100-4. 10.1016/j.jmr.2007.01.020.
- [4] J. R. Moser, "Low-Frequency Shielding of a Circular Loop Electromagnetic Field Source," *IEEE Transactions on Electromagnetic Compatibility*, vol. 9, no. 1, pp. 6-18, March 1967, doi: 10.1109/TEM.1967.4307447.
- [5] H. Y. Carr and E.M. Purcell, "Effects of diffusion on free precession in nuclear magnetic resonance experiments," *Phys. Rev.*, Vol. 94, pp. 630-638, 1954.
- [6] S. Meiboom and D. Gill, "Modified spin-echo method for measuring nuclear relaxation times," *Rev. Sci. Instrum.*, Vol. 29, pp. 688-691, 1958.
- [7] Clevan Lamason, Bryce MacMillan, Bruce Balcom, Brigitte Leblon, and Zarin Pirouz (2017) Field Measurements of Moisture Content in Black Spruce Logs with Unilateral Magnetic Resonance. *Forest Products Journal*: **2017**, Vol. 67, No. 1-2, pp. 55-62.
- [8] Riggan, M. T., Sharp, A. R., Kaiser, R., & Schneider, M. H. (1979). Transverse NMR relaxation of water in wood. *Journal of Applied Polymer Science*, 23(11), 3147-3154.
- [9] Menon, R. S., MaCkay, A. L., Hailey, Bloom, M., Burgess, A. E., & Swanson, J. S. (1987). An NMR determination of the physiological water distribution in wood during drying. *Journal of Applied Polymer Science*, 33(4), 1141-1155.
- [10] Snelling, E.C. *Soft Ferrites: Properties and Applications*, 2nd Ed.; Butterworths: London, 1988; Chap. 2
- [11] van der Zaag, P.J. (1999). New views on the dissipation in soft magnetic ferrites. *Journal of Magnetism and Magnetic Materials*. Vol. 197-197, p. 315.

Figure captions

Figure 1. Simple sketch showing the relative placement of the linear unilateral magnet array, NMR detection coil and homogeneous static magnetic field sample volume. The homogenous static magnetic field volume is indicated by the axis system intersecting the single B_0 flux line that defines the \hat{z} direction. The \hat{h} direction corresponds to displacement normal to the unilateral magnet surface while the \hat{w} direction assigns the remaining axis along the width of the magnet. The sample standoff distance from the magnet is $h_1 + h_2$ while the standoff distance from the NMR detection coil is h_2 . The direction of the rf fields provided by a loop or DD coil are also included. This work endeavors to develop NMR detection coils that have the distance h_1 minimized to maximize the distance h_2 and thus improve sample standoff distance.

Figure 2. A simple graphical model for the generation of the eddy current reduced rf field is shown in (a). Here the primary B_1 field from a circular loop induces eddy currents I_{eddy} on the conductor surface that concomitantly produce a field B_{eddy} that subtracts from B_1 . The plots in (b) for the rf field at a distance $h_2 = 1$ cm from the $R = 2$ cm circular loop coil surface as a function of r in free space or $h_1 = 4$ cm is shown as the solid line while the dashed line shows what happens when the conducting surface is moved closer to $h_1 = 2$ mm. The plots in (c) show the standoff distance dependence of the rf field developed by the same circular loop coil at the center $r = 0$ as a function of h_2 . Again the free space rf field with $h_1 = 4$ cm is shown as the solid line while moving the conductor closer to $h_1 = 2$ mm produces the dashed line. These plots were generated from the analytical results of Moser.

Figure 3. Simple sketch describing how an orthogonal bucking coil can be added in the h - z plane below the z - w surface of a DD coil. The counter-wound nature of the DD coil produces the primary field B_1 while the bucking coil yields B_{buck} . It is clear from this sketch that B_{buck} decreases B_1 below the z - w plane and increases B_1 above the plane. The gray region occupying the z - w plane represents the conducting unilateral magnet surface.

Figure 4. Summary of ANSYS developed numerical rf field calculations for a square loop, a bucked square loop, a DD coil and a bucked DD coil in (a) – (d) respectively. The left and center column show the rf fields

perpendicular to the \hat{z} direction and in the h-w plane without and with a conducting surface placed $h_1 = 6$ mm below the top of the rf coil complex. The right column shows the standoff performance of the coils obtained in the \hat{h} direction at the $z = w = 0$ center of the rf coil. The solid and dashed lines show the rf field value without and with the conducting surface as a function of distance h_2 from the coil surface. The vertical gray line shows the position of the homogenous static magnetic field volume where the shielding performance is evaluated.

Figure 5. Simple sketch describing how the rf field from a solenoid coil placed sideways on a conducting surface increases the rf field in the homogeneous static magnetic field volume above the coil. The solid black flux line describes the primary field of the solenoid coil while the flux line for the eddy current I_{eddy} generated rf field B_{eddy} enhances the rf field in the sample region. Again, the static magnetic field is in the \hat{z} direction.

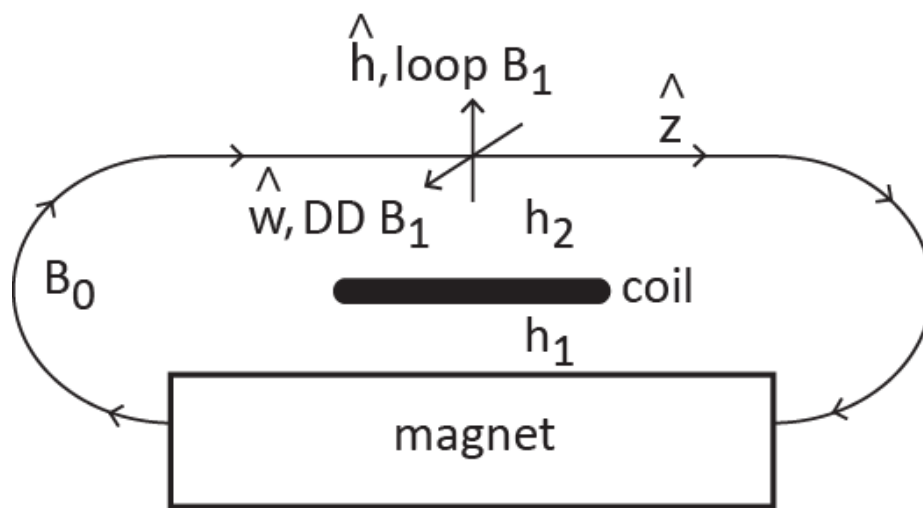
Figure 6. Summary of ANSYS developed numerical rf field calculations for a fringe and split fringe coil in (a) and (b) respectively. The left and center column show the rf fields perpendicular to the \hat{z} direction without and with a conducting surface placed $h_1 = 6$ mm below the top of the rf coil complex. The top and bottom rows in (a) and (b) respectively correspond to the rf field calculated in the h-w and h-z planes. The right column shows the standoff performance of the coils obtained in the \hat{h} direction at the $z = w = 0$ center of the rf coil. The solid and dashed lines show the rf field value without and with the conducting surface as a function of distance h_2 from the coil surface. The vertical gray line shows the position of the homogenous static magnetic field volume where the shielding performance is evaluated.

Figure 7. Magnetic resonance images obtained at a 4 MHz ^1H Larmor frequency for a large beaker of mineral oil placed on the surface of a similarly sized square loop coil, a fringe coil and a split fringe coil in (a) – (c) respectively. The images in the right column include an aluminum plate placed $h_1 = 6$ mm below the top of the rf coil while the images in the left column have the aluminum plate removed. The number inset on the lower right corner of the images in the right column is the ratio of the maximum signals obtained with and without the conducting plate.

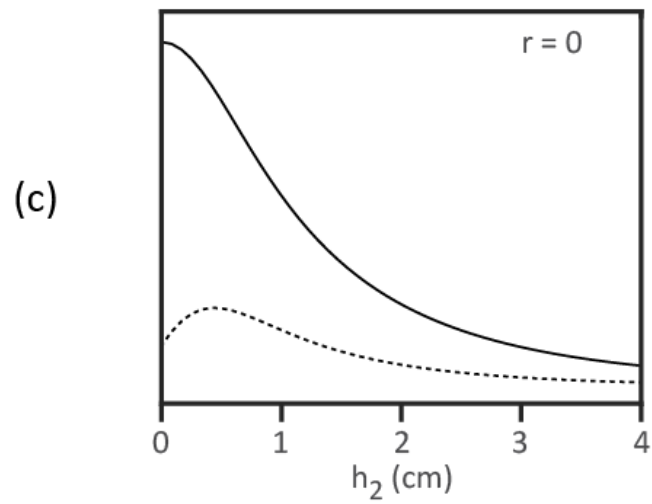
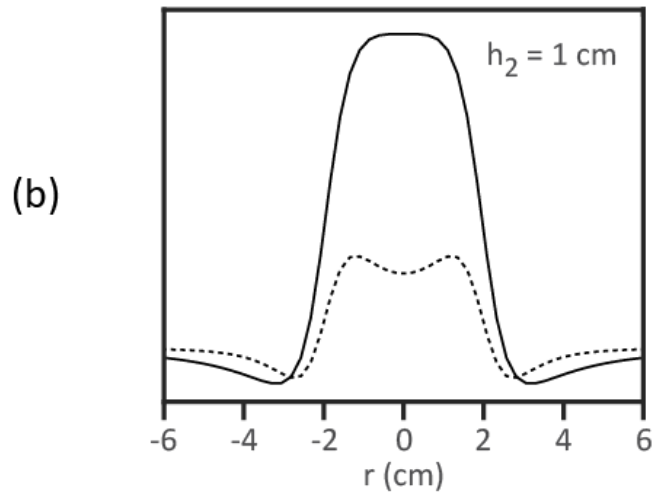
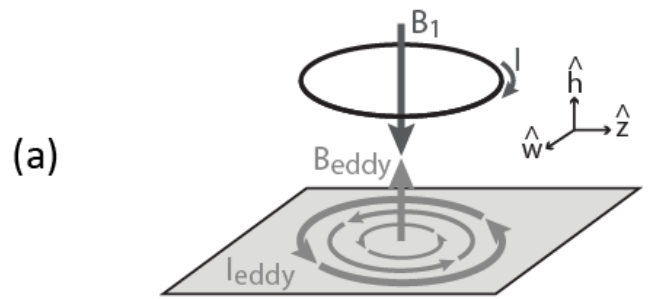
Figure 8. A large beaker of light mineral oil was placed on the magnet and coil assembly and CPMG experiments were run with the beaker lifted to varying standoff heights from the surface of the magnet and coil assembly. Experiments at different heights were analyzed for a single T_2^{obs} component and 95% confidence interval using the Matlab™ fit function. Results were plotted here for both the flat fringe coil (a) and the split fringe coil (b). As expected, the uncertainty increases as standoff distance increases, but the split fringe coil outperforms the simple flat fringe at every distance. At 2.1 cm standoff, the flat fringe coil produced data that was too noisy to be fit. All pulse sequence parameters were identical between the two sets of experiments.

Figure 9. A spin echo detected rf nutation experiment. Here, the rf pulse lengths were varied (x axis) and the resulting spin echo signal was integrated over the entire acquisition window (y axis). The experiments were run for both the fringe coil (a) and the split fringe coil (b), and then repeated five times for each to obtain a 95% confidence interval, shown as the thickness of the shaded lines. Data was integrated for magnitude, imaginary, and real data, displayed here as dark, medium, and light gray lines. All pulse sequence parameters were identical between the two sets of experiments.

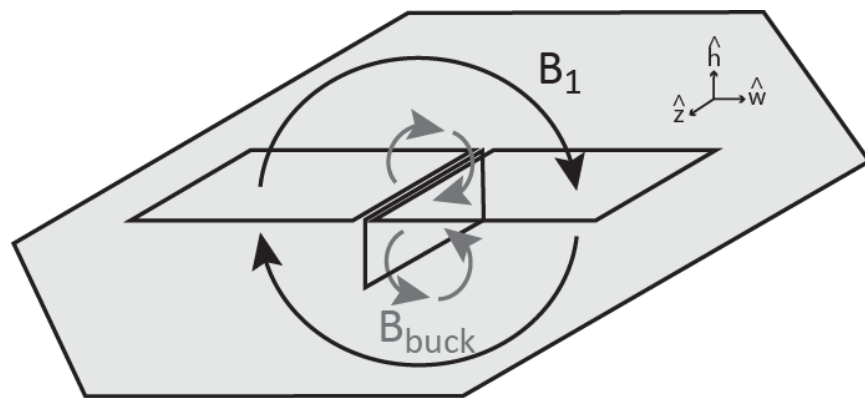
Figure 10. Examples simulating real applications of the split fringe coil. The fringe coil inserts into the existing groove of a BA11-4 unilateral magnet. The split fringe coil/unilateral magnet complex is placed into a water tight Pelican™ box lined with copper as shown in the picture on the left in (a). The enclosed NMR sensor was dunked into a bucket of laundry detergent, doped with CuSO_4 , as shown in the upper right in (a). This configuration resulted in the CPMG decay curve and ILT estimate of $T_2^{\text{obs}} = 16$ ms shown in (b). The CPMG decay in (c) corresponds to the small stick shown on the top of the magnet in the lower right of (a). The ILT in (c) reports two T_2^{obs} values, 3.5 ms and 20 ms for water in the cells and lumen, respectively.



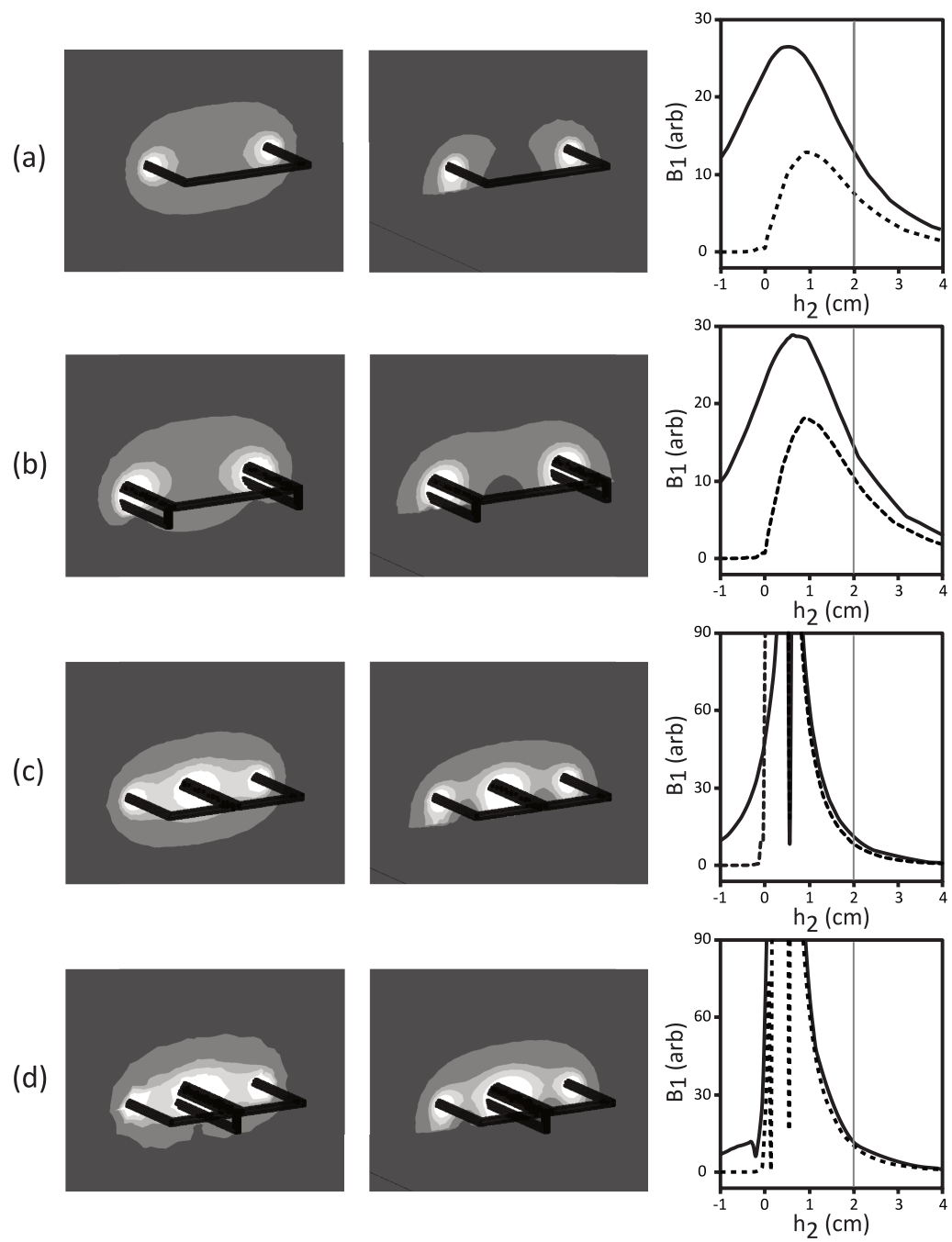
Gruber et al.
Figure 1



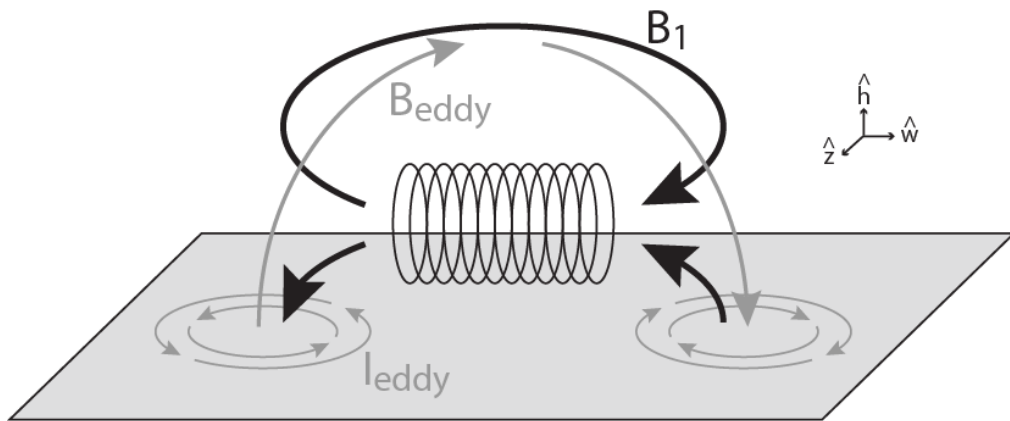
Gruber et al.
Figure 2



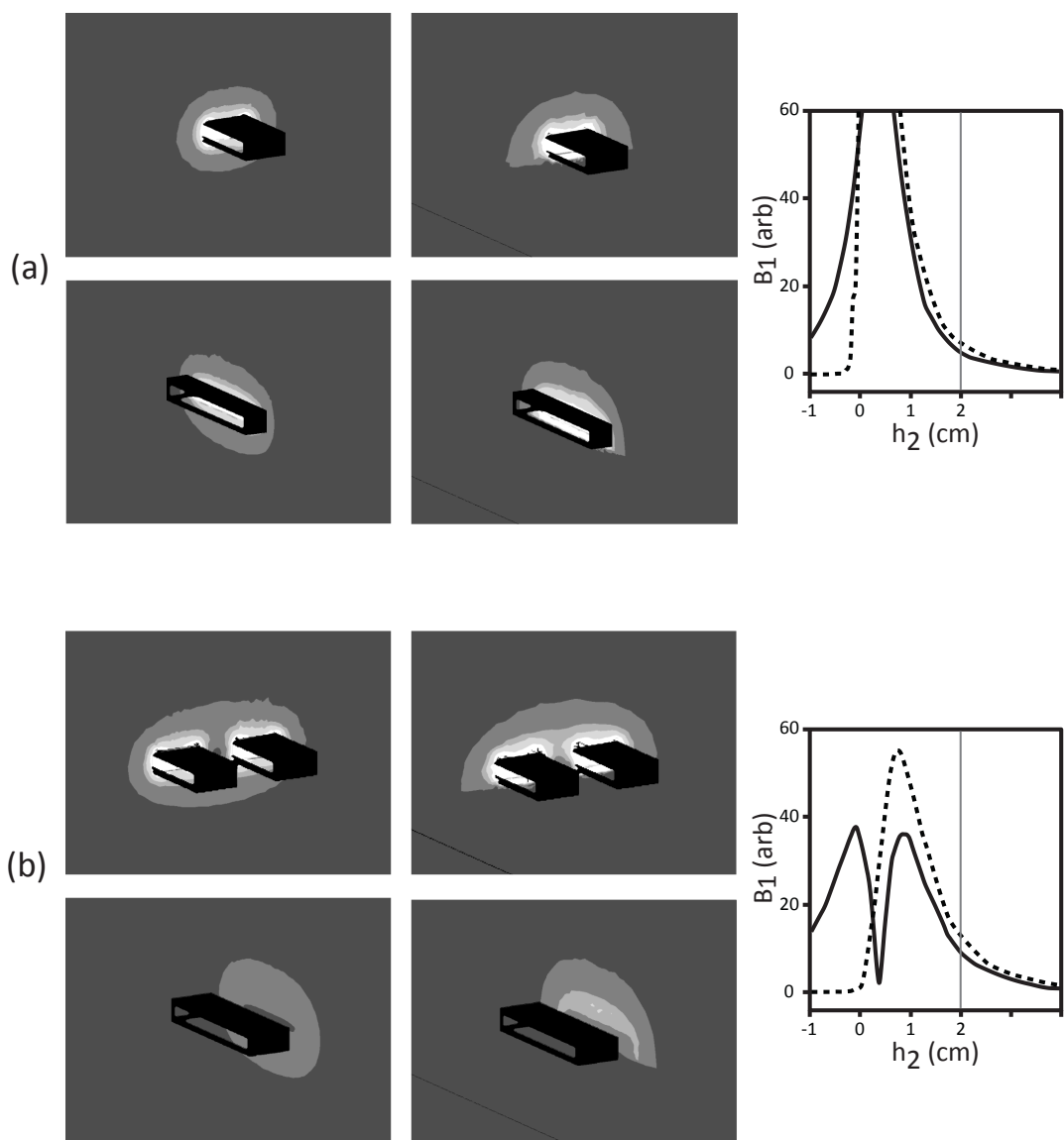
Gruber et. al.
Figure 3



Gruber et. al.
Figure 4

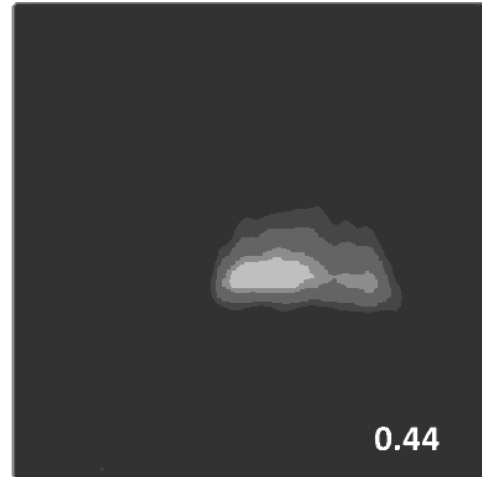
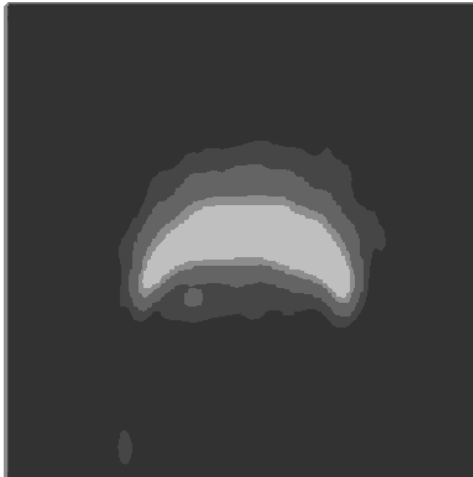


Gruber et. al.
Figure 5

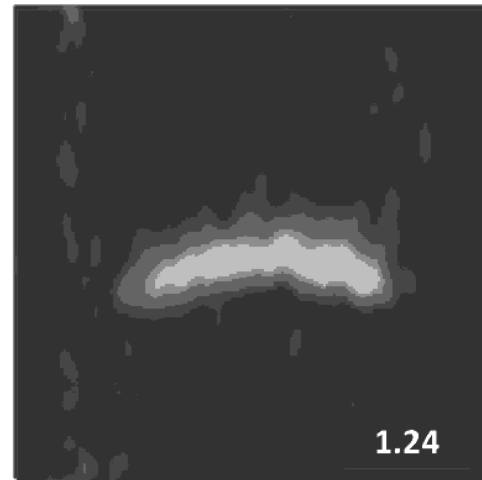
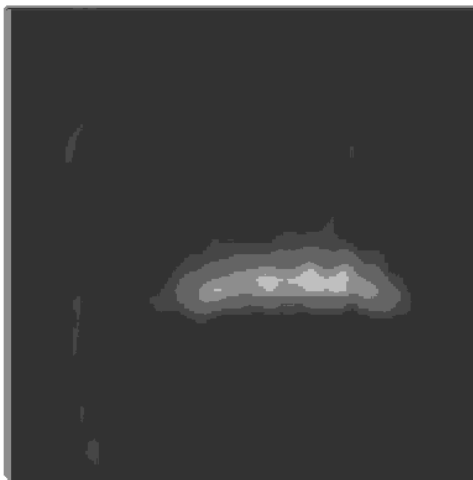


Gruber, D., et. al.
Figure 6

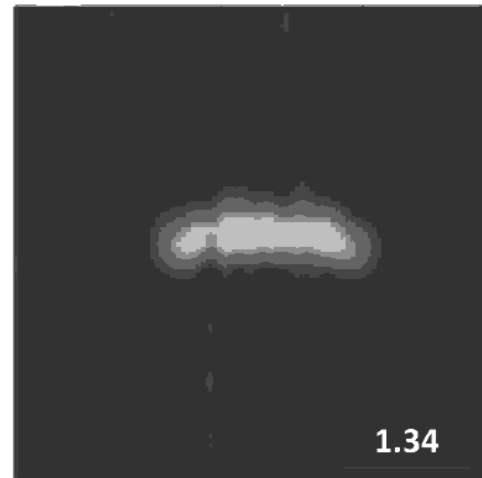
(a)



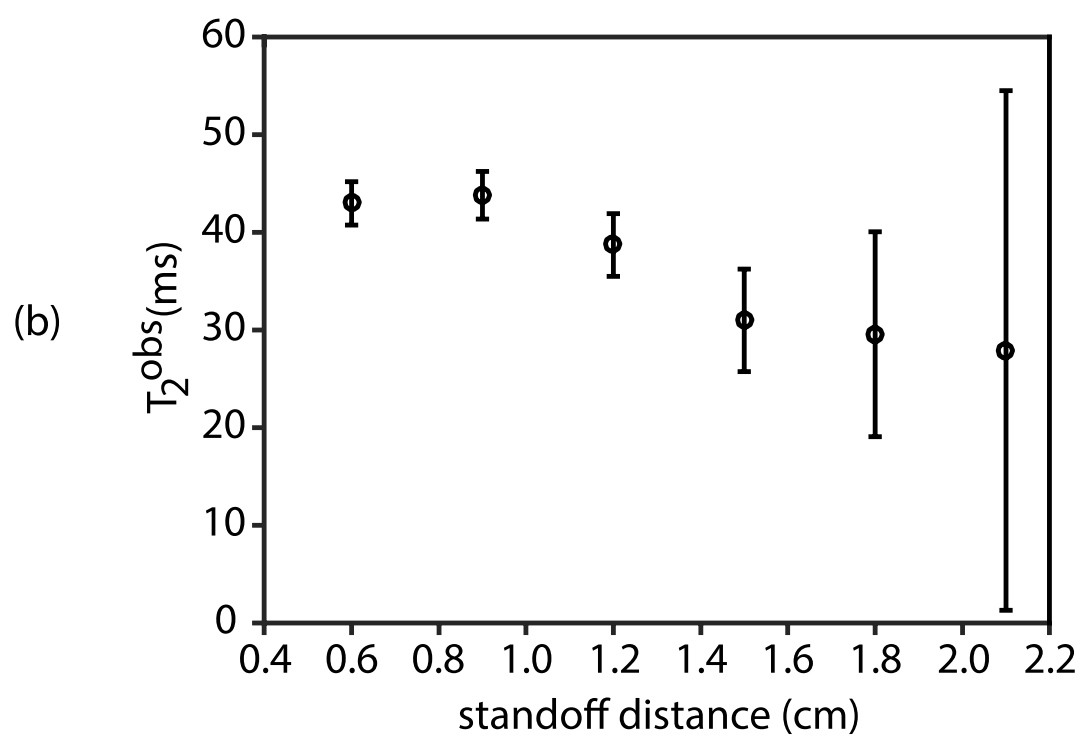
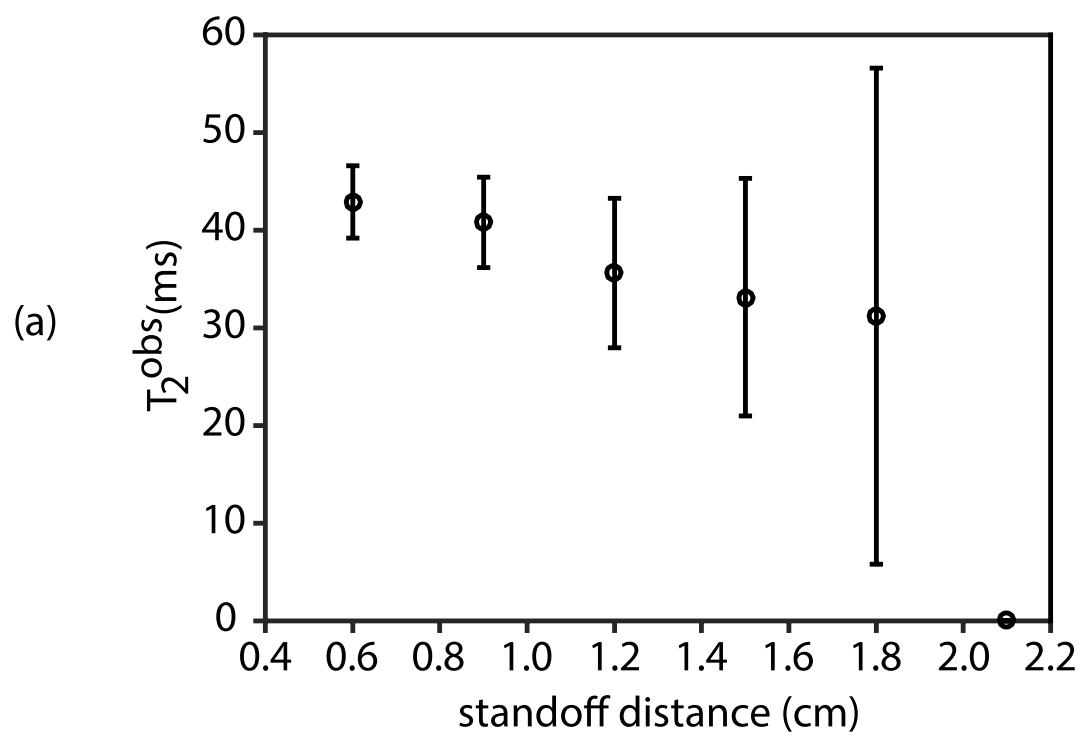
(b)



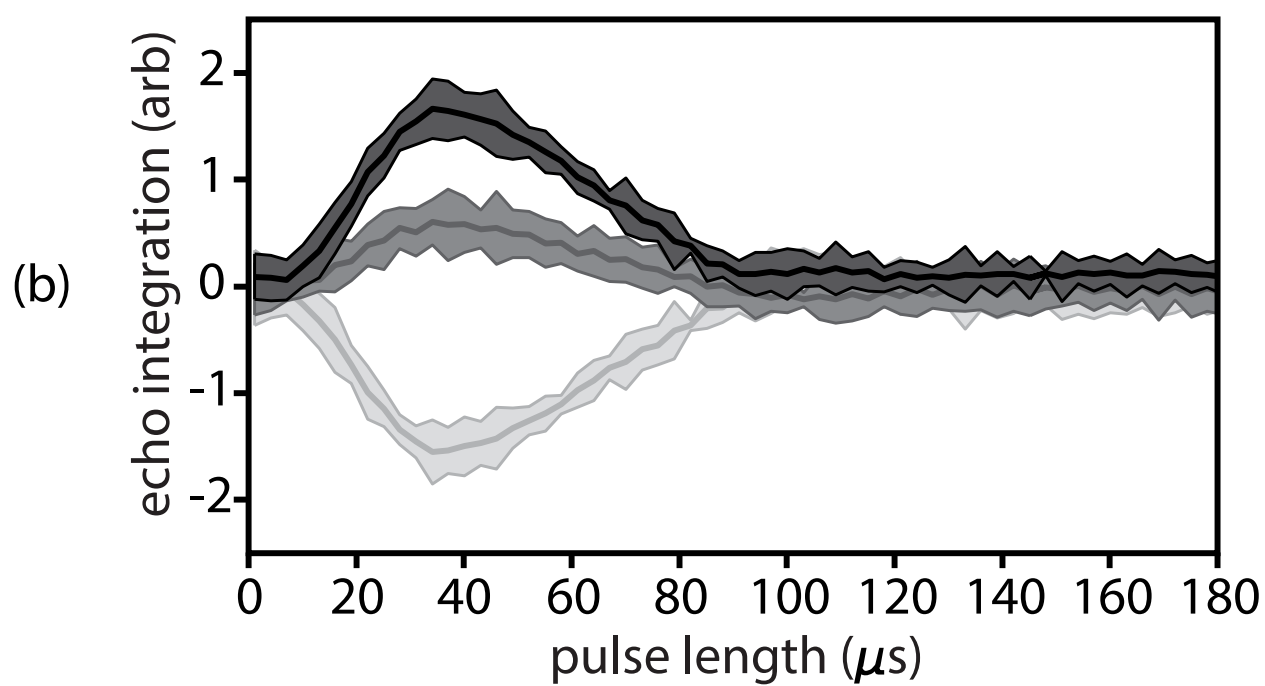
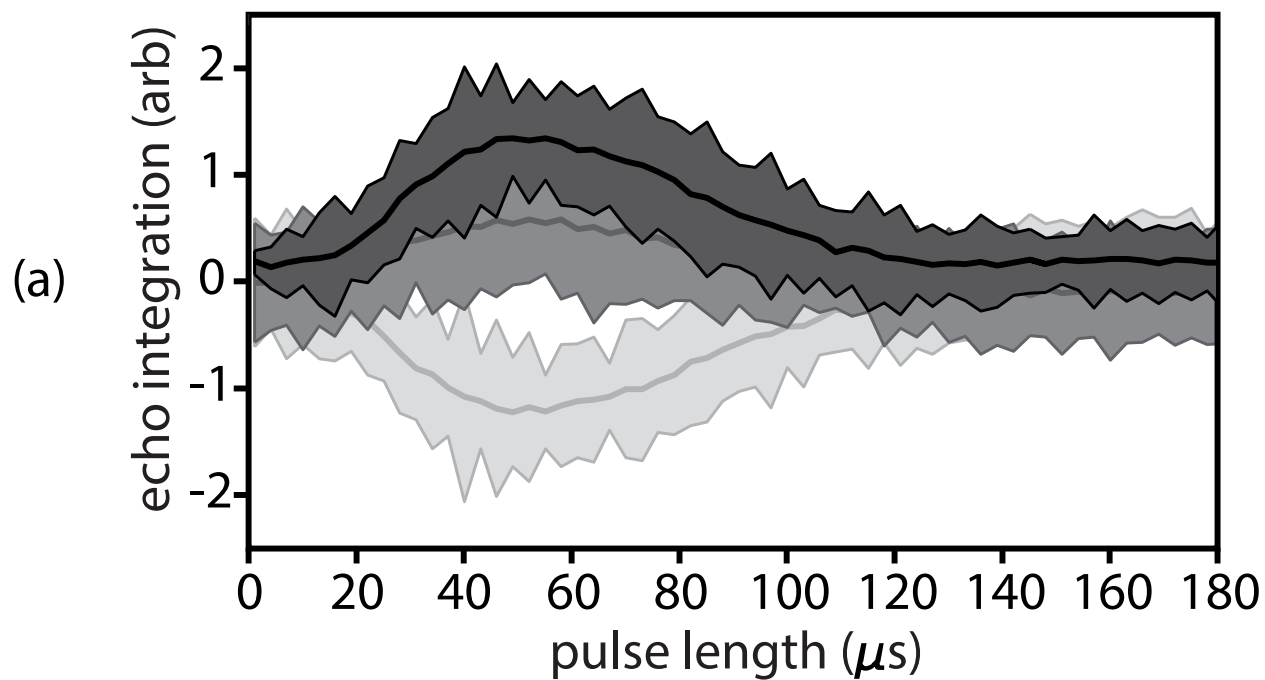
(c)



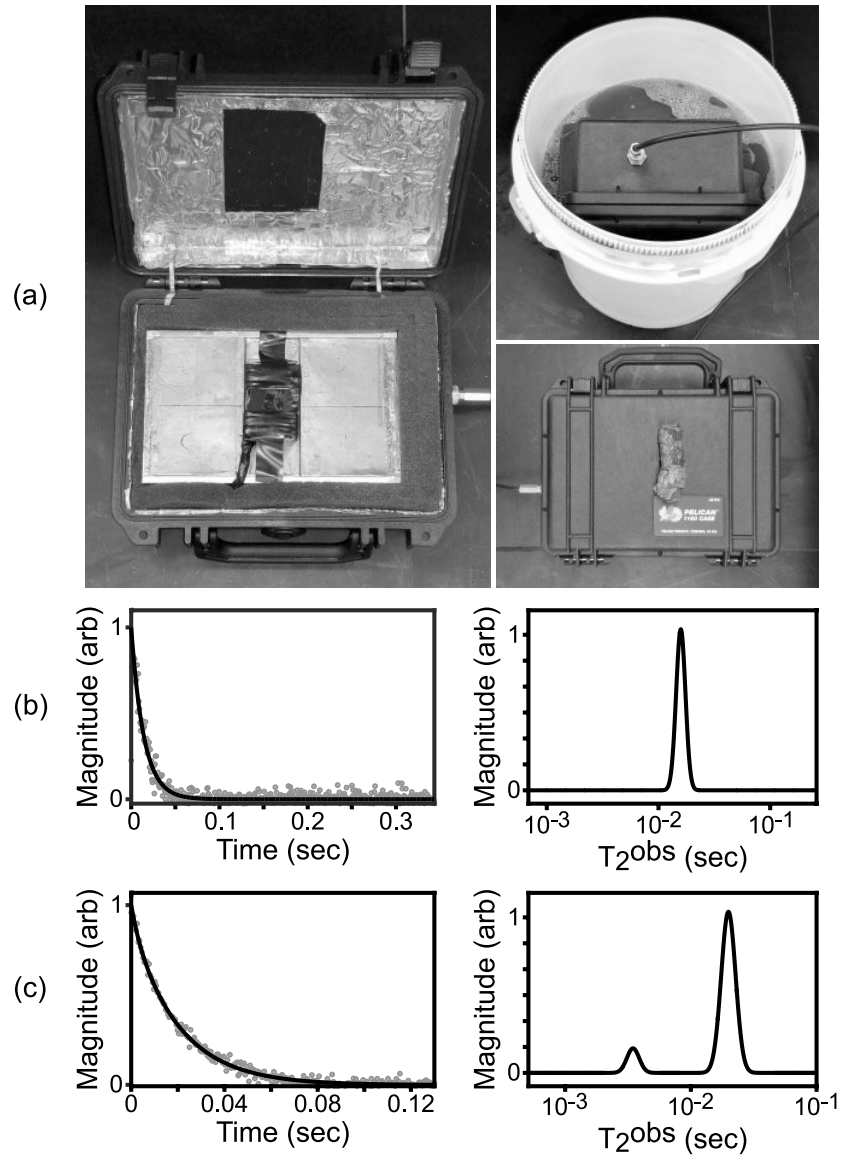
Gruber et. al.
Figure 7



Gruber et. al.
Figure 8



Gruber et. al.
Figure 9



Gruber et. al.
Figure 10